Commun Nonlinear Sci Numer Simulat 17 (2012) 2031–2044

Contents lists available at ScienceDirect

Commun Nonlinear Sci Numer Simulat

journal homepage: www.elsevier.com/locate/cnsns

Gyroaverage effects on nontwist Hamiltonians: Separatrix reconnection and chaos suppression

D. del-Castillo-Negrete [a,*], J.J. Martinell [b]

[a] Oak Ridge National Laboratory, Oak Ridge, TN, USA
[b] Institute of Nuclear Sciences, Universidad Nacional Autónoma de México, Mexico

ARTICLE INFO

Article history:
Available online 23 July 2011

We dedicate this paper to Phil Morrison on the occasion of his 60th birthday.

Keywords:
Hamiltonian chaos
Nontwist systems
Plasma physics

ABSTRACT

A study of finite Larmor radius (FLR) effects on $\mathbf{E}\times\mathbf{B}$ test particle chaotic transport in non-monotonic zonal flows with drift waves in magnetized plasmas is presented. Due to the non-monotonicity of the zonal flow, the Hamiltonian does not satisfy the twist condition. The electrostatic potential is modeled as a linear superposition of a zonal flow and the regular neutral modes of the Hasegawa–Mima equation. FLR effects are incorporated by gyro-averaging the $\mathbf{E}\times\mathbf{B}$ Hamiltonian. It is shown that there is a critical value of the Larmor radius for which the zonal flow transitions from a profile with one maximum to a profile with two maxima and a minimum. This bifurcation leads to the creation of additional shearless curves and resonances. The gyroaveraged nontwist Hamiltonian exhibits complex patterns of separatrix reconnection. A change in the Larmor radius can lead to heteroclinic–homoclinic bifurcations and dipole formation. For Larmor radii for which the zonal flow has bifurcated, double heteroclinic–heteroclinic, homoclinic–homoclinic and heteroclinic–homoclinic separatrix topologies are observed. It is also shown that chaotic transport is typically reduced as the Larmor radius increases. Poincare sections show that, for large enough Larmor radius, chaos can be practically suppressed. In particular, changes of the Larmor radius can restore the shearless curve.

1. Introduction

The study of particle transport in plasmas in the presence of strong magnetic fields is usually based on the $\mathbf{E}\times\mathbf{B}$ approximation that follows the particles' guiding centers and neglects the fast gyration on the magnetic field. However, for relatively high energy particles, or fields varying relatively rapidly in space, it is necessary to go beyond this approximation and incorporate finite Larmor radius (FLR) effects. The goal of this paper is to study the role of these effects on chaotic transport in the presence of drift waves on non-monotonic zonal shear flows.

Because of the non-monotonicity of the zonal flow, the guiding center Hamiltonian violates the twist condition. As we will review in the next section, nontwist Hamiltonian systems exhibit a rich phenomenology regarding their phase space structure and their chaotic transport properties. This type of Hamiltonian systems have found applications in many areas. Some examples include: magnetic fields with reverse shear in toroidal plasma devices of interest to control nuclear fusion [1–6]; modeling of transport by traveling waves in shear flows in fluids [7–9]; wave-particle interactions [10]; ray propagation in waveguides [11]; superconducting quantum interference devices (SQUIDs) [12]; relativistic dynamics of periodically driven oscillators [13]; self-consistent transport in Hamiltonian mean-field models [14]; and $\mathbf{E}\times\mathbf{B}$ transport in magnetized plasmas [15–17].

* Corresponding author.
E-mail address: delcastillod@ornl.gov (D. del-Castillo-Negrete).

1007-5704/$ - see front matter © 2011 Elsevier B.V. All rights reserved.
doi:10.1016/j.cnsns.2011.07.020

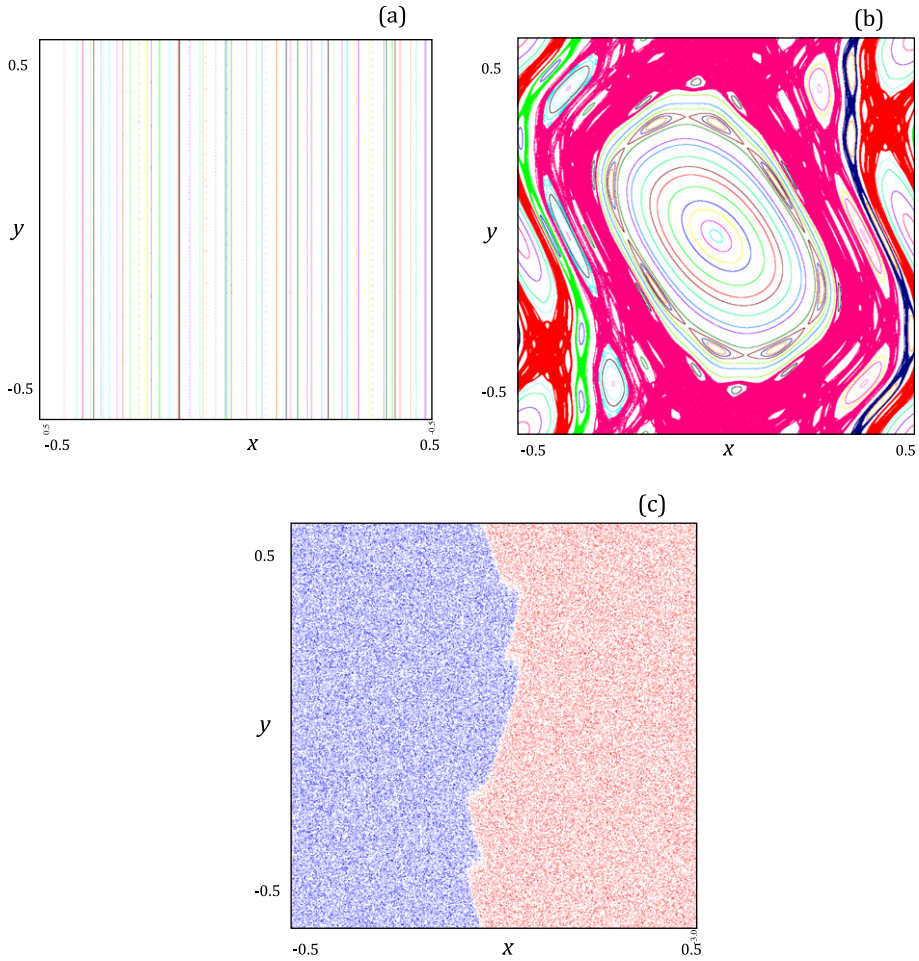

Fig. 1. Transition to chaos in Hamiltonian systems. (a) Standard map in the integrable limit; (b) Standard map at the threshold for global chaotic transport; (c) Standard non-twist map at the threshold for global chaotic transport. In the absence of a perturbation, the system is integrable and all orbits consist of invariant KAM circles depicted as vertical lines in (a). When the perturbation breaks the integrability, the phase space exhibits an intricate, fractal-like pattern of invariant circles, islands, and chaotic regions as depicted in (b). As (c) shows, in nontwist maps, the shearless curve typically provides a very robust transport barrier separating strongly chaotic regions. The blue (red) points denote the Poincare plot tracing a single initial condition starting to the left (right) of the shearless curve.

In this paper, following Ref. [16], we construct the guiding center nontwist Hamiltonian as a superposition of a non-monotonic $\mathbf{E} \times \mathbf{B}$ zonal shear flow and regular neutral modes of the Hasegawa–Mima equation [18] describing plasma drift waves. FLR effects are incorporated through a gyroaverage [19,20] of the guiding center Hamiltonian. Previous studies on the role of FLR effects on test particle dynamics have considered the diffusive and non-diffusive transport properties. In particular, the dependence of the particle diffusivity on the Larmor radius in plasma turbulence was studied in Refs. [21,22]. Larmor radius effects on non-diffusive transport were studied in Ref. [23] for turbulent transport and in Ref. [24] for chaotic transport. Here we focus on the study of two novel problems: the role of FLR effects on separatrix reconnection and suppression of chaotic transport.

Separatrix reconnection is a global bifurcation of the phase space ubiquitous in nontwist Hamiltonian systems, see for example Refs. [25–29] and references therein. This bifurcation changes the topology of the separatrix from heteroclinic to homoclinic. The term topology in this context refers to the qualitative different ways in which the stable and unstable manifolds link the unstable fixed points of the single mode integrable Hamiltonian. In the heteroclinic topology the unstable manifold of a fixed point joints the stable manifold of a different fixed point, whereas in the homoclinic topology the unstable manifold of a fixed point joints the stable manifold of the same fixed point. The bifurcation threshold of the heteroclinic-to-homoclinic transition can be computed by comparing the values of the level sets of the integrable Hamiltonian at the hyperbolic fixed points, or by comparing the direction of the eigenvectors of the hyperbolic fixed points involved in the reconnection process [28]. In this paper we show that gyroaveraged nontwist Hamiltonians exhibit complex patterns of separatrix reconnection. A change in the Larmor radius can lead to heteroclinic–homoclinic bifurcations and dipole formation. In addition, for large enough Larmor radii, the phase space can exhibit double heteroclinic–heteroclinic, homoclinic–homoclinic, and heteroclinic–homoclinic topologies.

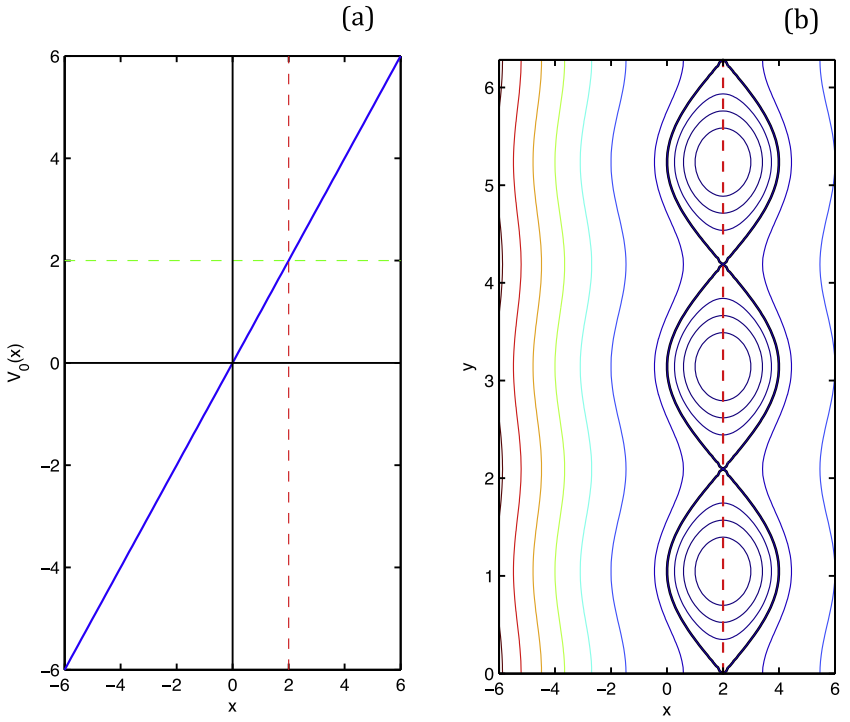

Fig. 2. Typical phase space portrait of integrable twist Hamiltonians with a single mode in the co-moving reference frame. Panel (a) shows a monotonic, linear zonal flow profile, $V_0(x) = x$. This flow corresponds to the unperturbed frequency in Eq. (3) which in this case satisfies the twist condition in Eq. (5). The dashed line indicates the location of the resonance, i.e. the region where the frequency of the single mode perturbation matches the frequency of the zonal flow. Panel (b) shows a contour plot of the twist Hamiltonian $H = x^2/2 + \cos(3y) - 2x$. The perturbation opens one chain of islands at the resonance. Because of the twist condition, in this case the separatrix topology is heteroclinic, i.e., the separatrix joins different hyperbolic points.

Chaotic transport has been a topic of significant interest in Hamiltonian systems in general. Nontwist systems are particularly interesting because, as shown in Refs. [1,7,28], shearless curves in these systems provide very robust transport barriers. By a robust transport barrier we mean an invariant circle that persists even though nearby invariant circles and high order islands have been destroyed as shown in the standard non-twist map example in Fig. 1(c). By contrast, as the standard twist map example in Fig. 1(b) illustrates, in twist maps all transport barriers are typically destroyed before chaos is widespread in the phase space. That is, before a significant fraction of the fixed points have lost stability and the corresponding islands have been destroyed. Other works on chaotic transport in nontwist maps include: renormalization group studies [30,31]; analysis of the barrier escape time and barrier transmissivity [32]; KAM theory and partial justification of the Greene's criterion for nontwist Hamiltonians [33,34]; and use of indicator points to determine the location of the shearless curve [35], among others. In this paper we show that chaotic transport is typically reduced as the Larmor radius increases, and for large enough Larmor radius, chaos can be practically suppressed. In particular, we show that small changes on the Larmor radius can restore a broken shearless curve.

The organization of the rest of this paper is as follows. The next section reviews basic concepts of nontwist Hamiltonian systems. The construction of the nontwist gyroaveraged Hamiltonian is presented in Section 3. Section 4 presents the main results on the FLR effects on separatrix reconnection and chaotic transport. The conclusions are presented in Section 5.

2. Nontwist Hamiltonian systems

Let $H_0 = H(q,p)$ be an integrable, one-degree-of-freedom Hamiltonian system, and consider

$$H = H_0(q,p) + H_1(q,p,t). \tag{1}$$

As it is well-known, depending on the perturbation, $H_1(q,p,t)$, the dynamical system in Eq. (1) can cease to be integrable, i.e., the system can exhibit chaos. To study the transition to chaotic dynamics it is convenient to use the canonical action-angle coordinates (J,θ) of H_0. By construction, H_0 depends only on J, and the solution of the integrable problem reduces to

$$J = J_0, \quad \theta = \theta_0 + \Omega(J_0)t, \tag{2}$$

where (J_0,θ_0) is the initial condition, and the unperturbed frequency is

$$\Omega = \frac{\partial H_0}{\partial J}. \tag{3}$$

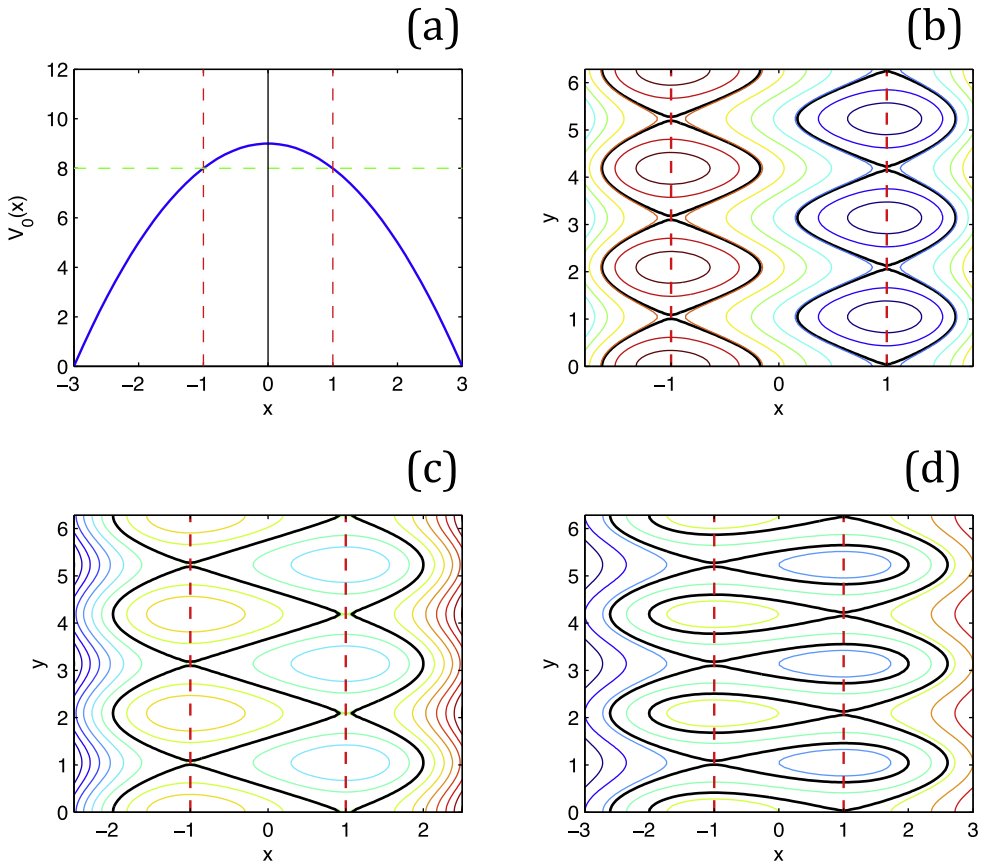

Fig. 3. Typical phase space portrait of integrable, nontwist Hamiltonians with a single mode. (a) non-monotonic, quadratic zonal flow profile, $V_0(x)$. The dashed lines indicate the locations of the resonances. Panels (b), (c) and (d) show contour plots of the nontwist Hamiltonian, $H = x - x^3/3 - b\cos(3y)$ for $b = 1/4$, $b = 2/3$ and $b = 1$ respectively. Because of the violation of the twist condition, contrary to the case of twist Hamiltonians shown in Fig. 2, one mode creates two chains of islands. In this case, the separatrix topology can be heteroclinic (b), i.e. the separatrix joins different hyperbolic points, or homoclinic (d), i.e. one branch of the separatrix joins the same hyperbolic point. Panel (c) shows the reconnection state at the threshold of the heteroclinic–homoclinic bifurcation.

In these variables, the perturbed Hamiltonian in Eq. (1) becomes

$$H = H_0(J) + H_1(J, \theta, t). \tag{4}$$

As Eq. (2) indicates, in the (J, θ) phase space, the orbits of H_0 are horizontal lines known as invariant circles or KAM (Kolmogorov–Arnold–Moser) curves (see Fig. 1). The problem of the transition to chaos consists of determining the fate of these invariant circles under the perturbation H_1. As Fig. 1 shows, in general, under the perturbation, the phase space exhibits an intricate mixture of smoothly deformed KAM curves, islands, and chaotic regions. Determining which orbits are simply deformed and which ones are destroyed is a highly non-trivial fascinating problem in Hamiltonian dynamical systems. Since the seminal work of Kolmogorov, Arnold, and Moser it is known that this problem depends, among other things, on the properties of the unperturbed frequency, Ω. In particular, one of the main lessons of the KAM theory (see, e.g., Refs. [36,37]) is that the persistence of an invariant circle with $J = J_0$ depends on the degree of irrationality (as measured by the rate of convergence of the continued fraction expansion) of $\Omega(J_0)$. This key intuition is the cornerstone of the extensively used Greene's residue criterion [38], which is a powerful numerical method to determine accurately and efficiently the threshold for the destruction of KAM circles.

A key assumption in the formulation of the standard version of the KAM theorem is the nondegeneracy condition, also known as the twist condition,

$$\frac{\partial \Omega}{\partial J} = \frac{\partial^2 H_0}{\partial J^2} \neq 0, \quad \forall J. \tag{5}$$

Although Hamiltonians of the form $H_0 = p^2/2 + V(q)$ satisfy this condition, there are Hamiltonians for which this is not the case. Hamiltonians that do not satisfy the twist condition in Eq. (5) are known as nontwist Hamiltonians. As discussed in

the introduction, this type of Hamiltonian naturally appears in transport problems in fluid mechanics, plasma physics, and condensed matter physics. Of particular interest in nontwist systems is the study of shearless curves. In the integrable limit, a shearless curve is an invariant circle with a local maximum (or minimum) of the frequency Ω. That is, an invariant circle going through $J = J_0$ such that $\partial_J \Omega(J_0) = 0$. Under the effect of a perturbation, the shearless curve can survive as a deformed smooth curve or it can break into the stochastic region. However, the transition to chaos of the shearless curve is different than the transition to chaos of KAM curves in twist systems [7,28]. In particular, as illustrated in Fig. 1, shearless curves are very robust transport barriers. At a more fundamental level, it has been shown that at the transition point, the self-similar critical behavior of shearless KAM curves in nontwist systems belong to a universality class different than the universality class of the twist systems [30]. Beyond the robustness properties of shearless curves under non-integrable perturbations, the phase space of nontwist Hamiltonians is fundamentally different than that of twist Hamiltonians. In particular, as illustrated in Fig. 3, nontwist Hamiltonians can exhibit a global bifurcation known as separatrix reconnection. The onset of this bifurcation depends on the amplitude of the perturbation (that determines the size of the resonances) and the frequency of the perturbation (that determines the location of the resonance layers with respect to the maximum of the unperturbed frequency). Both, the robustness of the shearless curve and separatrix reconnection play a fundamental role on the study of transport in nontwist Hamiltonians.

3. Gyro-averaged nontwist E × B Hamiltonian

We consider test particle transport in strongly magnetized plasma. Using a cartesian coordinate system, the magnetic field is assumed constant and pointing in the z-direction. When finite Larmor radius (FLR) effects are neglected, the dynamics are determined by the drift equation

$$\frac{d\mathbf{r}}{dt} = \frac{\mathbf{E}\times\mathbf{B}}{B^2}, \tag{6}$$

that follows the particle's guiding center, $\mathbf{r} = (x,y)$, in the $\mathbf{E}\times\mathbf{B}$ approximation where $\mathbf{E}$ is the electrostatic field, and $\mathbf{B}$ is the magnetic field. Writing $\mathbf{B} = B_0\hat{\mathbf{z}}$, and $\mathbf{E} = -\nabla\phi(x,y,t)$, Eq. (6) can be equivalently written as the Hamiltonian dynamical system

$$\frac{dx}{dt} = -\frac{\partial\phi}{\partial y}, \quad \frac{dy}{dt} = \frac{\partial\phi}{\partial x}, \tag{7}$$

where the electrostatic potential is the Hamiltonian, and the spatial coordinates (x,y) are the canonical conjugate phase space variables.

For relatively high energy particles the zero Larmor radius approximation fails and it is necessary to incorporate FLR effects. A simple, natural way of doing this is to substitute the $\mathbf{E}\times\mathbf{B}$ flow on the right hand side of Eq. (7), which is evaluated at the location of the guiding center, by its gyroaverage over a ring of radius ρ, where ρ is the Larmor radius [19,20]. This approximation is valid provided the gyrofrequency is greater than other frequencies in the system and yields the following gyroaveraged Hamitonian system

$$\frac{dx}{dt} = -\left\langle\frac{\partial\phi}{\partial y}\right\rangle_\theta = -\frac{\partial}{\partial y}\langle\phi\rangle_\theta, \tag{8}$$

$$\frac{dy}{dt} = \left\langle\frac{\partial\phi}{\partial x}\right\rangle_\theta = \frac{\partial}{\partial x}\langle\phi\rangle_\theta, \tag{9}$$

where the gyroaverage, $\langle\rangle_\theta$, is defined as

$$\langle\Psi\rangle_\theta \equiv \frac{1}{2\pi}\int_0^{2\pi}\Psi(x+\rho\cos\theta, y+\rho\sin\theta)d\theta. \tag{10}$$

To obtain the electrostatic potential, ϕ, we start from the Hasegawa–Mima model [18] describing drift waves in magnetized plasmas

$$[\partial_t + (\mathbf{z}\times\nabla\phi)\cdot\nabla](\nabla^2\phi - \phi - \beta x) = 0, \tag{11}$$

where the x coordinate corresponds to the direction of the density gradient driving the drift-wave instability, and y corresponds to the direction of propagation of the drift-waves, in the slab approximation. In toroidal geometry, x is analogous to a normalized coordinate along the minor radius, y is a poloidal-like coordinate, and, in the tokamak ordering, z corresponds to the toroidal direction. The parameter $\beta = n_0(x)'/n_0(x)$ measures the scale length of the density gradient.

Following Ref. [16] we construct ϕ using a linear superposition of drift-waves on a background zonal flow

$$\phi = \varphi_0(x) + \sum_{j=1}^{N}\varepsilon_j\varphi_j(x)\cos k_j(y - c_j t), \tag{12}$$

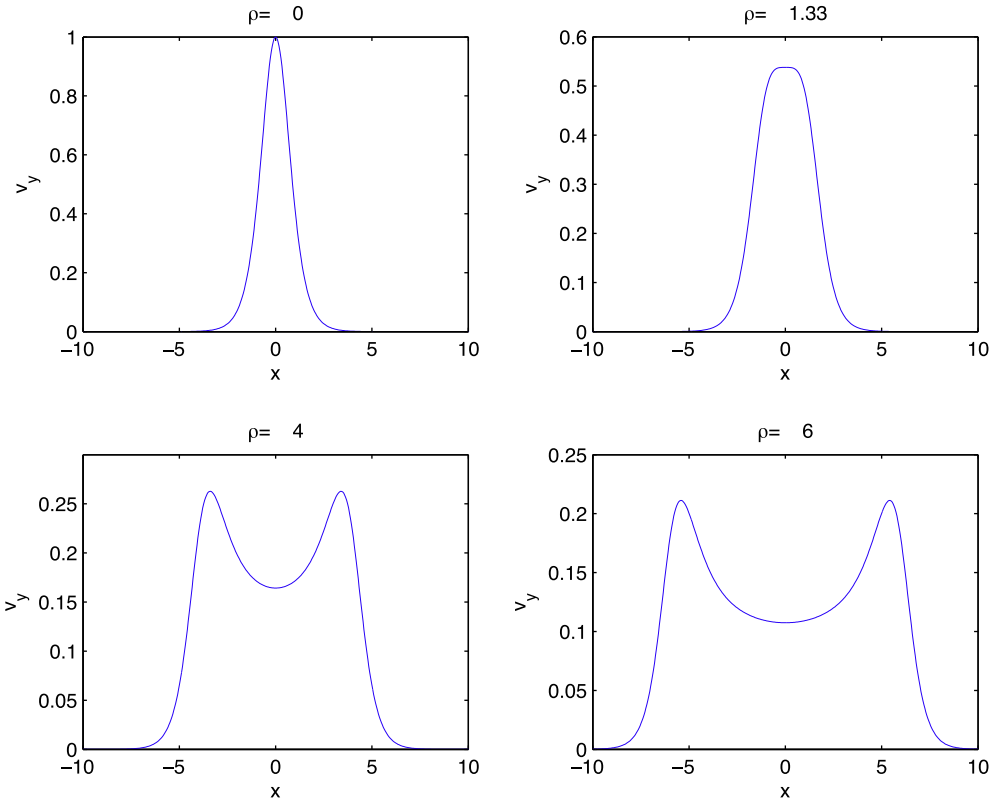

Fig. 4. Zonal shear flow profile for different values of ρ according to Eq. (25). For $0 \leqslant \rho < 1.33$ the zonal flow has a maximum at $x = 0$. However for $\rho \geqslant 1.33$ a bifurcation creates a minimum at $x = 0$ along with two symmetrically located maxima.

where the first term on the right hand side of (12) corresponds to an equilibrium zonal shear flow, and the second term is a superposition of regular neutral modes of Eq. (11). Going back to the discussion in the previous section, we identify the (x,y) coordinates with the action-angle coordinates (J,θ) and identify $\varphi_0(x)$ with the integrable part $H_0(J)$ of the perturbed Hamiltonian in Eq. (4). According to Eq. (7), the unperturbed frequency Ω in Eq. (3) corresponds to the $\mathbf{E}\times\mathbf{B}$ zonal flow, $\mathbf{u}_0 = u_0(x)\mathbf{e}_y = \mathbf{e}_z \times \nabla\varphi_0$, and the twist condition reduces to the condition of having a monotonic decreasing or monotonic increasing shear flow, i.e. $du_0/dx \neq 0$. However, here we are interested in the study of transport in non-monotonic $\mathbf{E}\times\mathbf{B}$ flows. As an specific example we consider

$$u_0 = \operatorname{sech}^2 x, \tag{13}$$

for which

$$\varphi_0(x) = \tanh x, \tag{14}$$

where x has been non-dimensionalized using the characteristic width, L, of the zonal flow. In this case there are two regular neutral modes with eigenfunctions

$$\varphi_{1,2}(x) = \operatorname{sech}^2 x, \tag{15}$$

and the $\mathbf{E}\times\mathbf{B}$ Hamiltonian in Eq. (12) becomes

$$\phi = \tanh x - \eta x + \epsilon_1 \operatorname{sech}^2 x \cos(k_1 y) + \epsilon_2 \operatorname{sech}^2 x \cos(k_2 y - \omega t), \tag{16}$$

where we have made a Galilean transformation to the co-moving reference frame of the first regular neutral mode. Further details on the linear eigenmode analysis and the construction of this model can be found in Ref. [16]. Note that, because $du_0/dx = -2\operatorname{sech}^2 x \tanh x = 0$ at $x = 0$, the Hamiltonian in Eq. (16) is a nontwist Hamiltonian.

The gyroaverage of Eq. (16) leads to the nontwist Hamiltonian

$$\langle\phi\rangle_\theta = M_\rho(x) - \eta x + \epsilon_1 I_{k_1\rho}(x)\cos(k_1 y) + \epsilon_2 I_{k_2\rho}(x)\cos(k_2 y - \omega t), \tag{17}$$

where the Larmor radius ρ has been non-dimensionalized using the characteristic width, L, of the zonal flow. Using this Hamiltonian in Eqs. (8) and (9) we get the following equations of motion

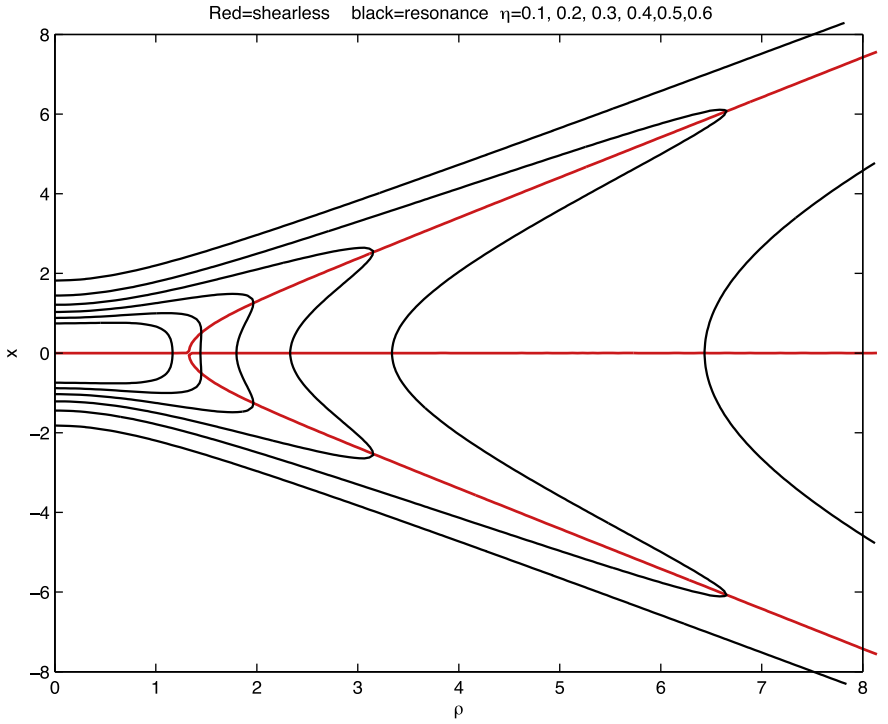

Fig. 5. Parametric dependence of the location of the shearless transport barrier (s) and resonances. The red curves correspond to $\sigma_0(x;\eta,\rho)=0$. The black curves correspond to $R(x;\eta,\rho)=0$ from left to right $\eta=0.6$, 0.5, 0.4, 0.3, 0.2 and 0.1.

$$\begin{aligned}\frac{dx}{dt}&=\epsilon_1 k_1 I_{k_1\rho}(x)\sin k_1 y+\epsilon_2 k_2 I_{k_2\rho}(x)\sin(k_2 y-\omega t),\\ \frac{dy}{dt}&=I_{0\rho}(x)-\eta-2\epsilon_1 K_{k_1\rho}(x)\cos k_1 y-2\epsilon_2 K_{k_2\rho}(x)\cos(k_2 y-\omega t),\end{aligned}\tag{18}$$

where the functions M_ρ, $I_{k\rho}$, and $K_{k\rho}$ are

$$M_\rho(x)=\frac{1}{\pi}\int_0^\pi \tanh(x-\rho\cos\theta)d\theta,\tag{19}$$

$$I_{k\rho}(x)=\frac{1}{\pi}\int_0^\pi \operatorname{sech}^2(x+\rho\cos\theta)\cos(k\rho\sin\theta)d\theta,\tag{20}$$

$$K_{k\rho}(x)=\frac{1}{\pi}\int_0^\pi \operatorname{sech}^2(x+\rho\cos\theta)\tanh(x+\rho\cos\theta)\cos(k\rho\sin\theta)d\theta.\tag{21}$$

In the small ρ limit,

$$M_\rho(x)=\tanh x-\frac{\rho^2}{2}\operatorname{sech}^2 x\tanh x+\mathcal{O}(\rho^3),\tag{22}$$

$$I_{k\rho}(x)=\left[1-\left(\frac{k^2}{4}-1+\frac{3}{2}\operatorname{sech}^2 x\right)\rho^2\right]\operatorname{sech}^2 x+\mathcal{O}(\rho^3),\tag{23}$$

$$K_{k\rho}(x)=\operatorname{sech}^2 x\tanh x\left[1-\rho^2\left(3\operatorname{sech}^2 x+\frac{k^2}{4}-1\right)\right]+\mathcal{O}(\rho^3).\tag{24}$$

4. Gyro-average effects on separatrix reconnection and chaos

Separatrix reconnection and the destruction of transport barriers of the $\rho=0$ nontwist $\mathbf{E}\times\mathbf{B}$ Hamiltonian in Eq. (16) has been studied before in Refs. [7,16]. In the rest of this paper we study the role of FLR effects on these problems.

4.1. Zonal flow and fixed points bifurcations

Fig. 4 shows the zonal flow of the gyroaveraged Hamiltonian,

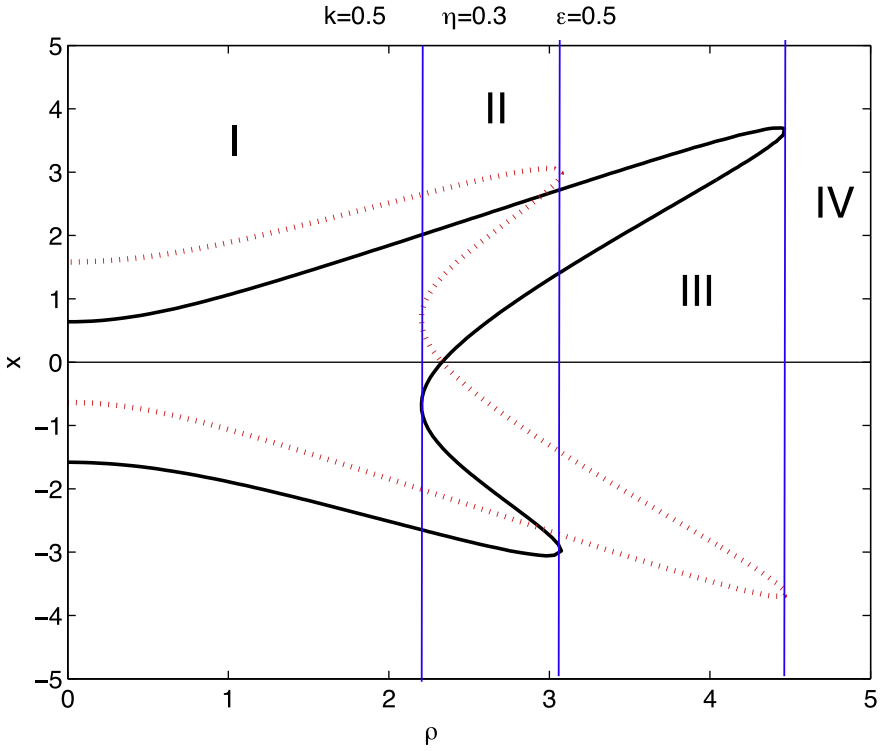

Fig. 6. Creation and annihilation of fixed points as function of the Larmor radius. The solid-black (dashed-red) curve tracks the x-location, x_*, of the fixed points of the single-mode gyroaveraged Hamiltonian in Eq. (27), with $k_1 = 0.5$, $\eta = 0.3$ and $\epsilon_1 = 0.5$, for n = even (n = odd) in Eq. (31). In regions I and III there are two fixed points in x_* for n odd and two for n even. However, in region II there are four fixed points in each case, and there are none in region IV. The transition from one region to the next is marked by bifurcations that create or annihilate pairs of fixed points in the phase space.

$$u_0(x) = \frac{\partial}{\partial x}\langle \varphi_0 \rangle_\theta = I_{0\rho}(x), \tag{25}$$

for different values of ρ. For $\rho = 0$, u_0 exhibits the expected $\mathrm{sech}^2 x$ profile with a single maximum at $x = 0$. However, for large enough values of ρ the zonal flow profile bifurcates and develops two maxima whose relative distance increases linearly with ρ. Zonal flow extrema are important because they correspond to shearless orbits. From the point of view of separatrix reconnection there is not a qualitative difference between shearless curves corresponding to minima and those corresponding to maxima of the zonal flows. However, shearless curves forming at inflection points of zonal flows can exhibit qualitatively different reconnection scenarios [26,27].

In the absence of perturbations, $\epsilon_1 = \epsilon_2 = 0$, these orbits are defined by the condition

$$\sigma_0(x;\eta,\rho) = \frac{\partial^2 \langle \phi_0 \rangle_\theta}{\partial x^2} = -2K_{0\rho}(x) = 0. \tag{26}$$

Fig. 5 shows the location of the unperturbed shearless orbits as function of ρ according to Eq. (26). Consistent with Fig. 4, for $\rho \leqslant 1.33$ there is only one shearless curve which corresponds to the single maximum of the zonal flow. However, for $\rho > 1.33$ the zonal flow bifurcates: the center becomes a minimum and two symmetrically located maxima are created. In this case, $\rho = 1.33$ defines a pitch-fork bifurcation that creates three shearless curves.

When a normal mode perturbation is added to the zonal flow, a chain of island forms at the resonance layer where the frequency of the normal mode matches the frequency of the zonal flow. In the case of a single mode Hamiltonian in the comoving reference frame,

$$\langle \phi \rangle_\theta = M_\rho(x) - \eta x + \epsilon_1 I_{k_1\rho}(x)\cos(k_1 y), \tag{27}$$

the resonance layer is defined by the condition

$$R(x;\rho,\eta) = \frac{\partial \langle \phi_0 \rangle_\theta}{\partial x} - \eta = I_{0\rho}(x) - \eta = 0. \tag{28}$$

The solid black lines in Fig. 5 tracks the location of the resonances as function of ρ for several values of η. Consistent with the fact that for small values of ρ the zonal flow has a single maximum, in this case there can be zero or at most two resonances. However, for large values of ρ, and small enough values of η, there can be up to four resonances.

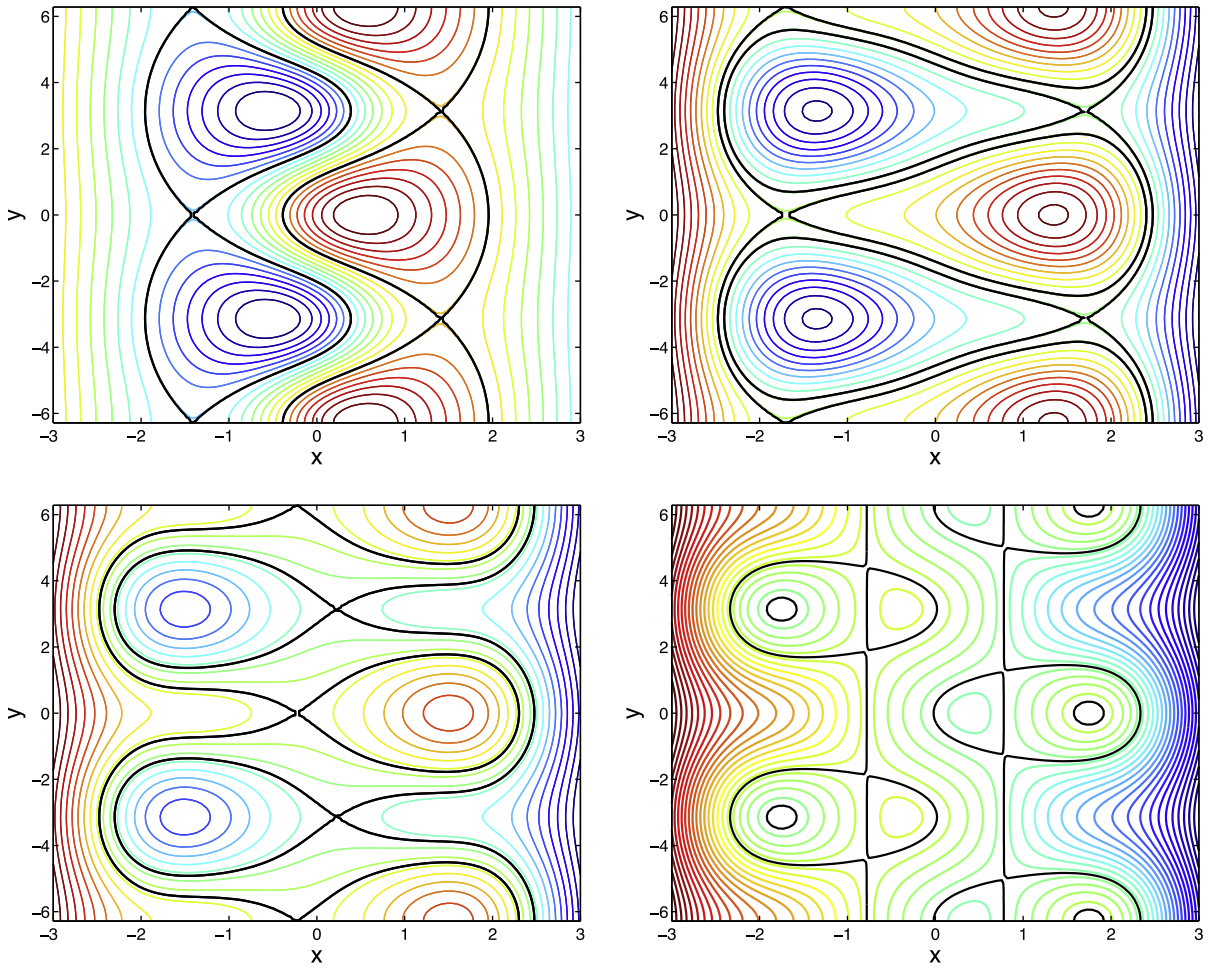

Fig. 7. Heteroclinic-homoclinic separatrix reconnection and dipole bifurcations for increasing values of the gyro-radius, ρ. The four panels show contour plots of the gyroaveraged Hamiltonian in Eq. (27) with $\epsilon_1 = 0.5$, $\eta = 0.4$, $k = 1$ and $\rho = 0$ (top left), $\rho = 1.5$ (top right), $\rho = 1.7$ (bottom left) and $\rho = 2$ (bottom right). The bold black line denotes the contour level of the separatrix.

For the single-mode Hamiltonian in Eq. (27), the fixed points (x_*, y_*) are defined by the condition $\partial_x\langle\phi\rangle_\theta(x_*, y_*) = \partial_y\langle\phi\rangle_\theta(x_*, y_*) = 0$ which according to Eq. (27) gives

$$I_{k_1\rho}(x_*)\sin k_1 y_* = 0, \tag{29}$$

$$I_{0\rho}(x_*) - \eta - 2\epsilon_1 K_{k_1\rho}(x_*)\cos k_1 y_* = 0. \tag{30}$$

One class of solutions to these equations is

$$y_* = n\pi/k_1, \quad \eta - I_{0\rho}(x_*) + (-1)^n 2\epsilon_1 K_{k_1\rho}(x_*) = 0. \tag{31}$$

Fig. 6 tracks the solutions, x_* for n odd and n even as function of the Larmor radius ρ. Four qualitatively different regions are identified. In regions I and III there are two fixed points in x_* for n odd and two for n even. However, in region II there are four fixed points in each case, and there are none in region IV. The transition from one region to the next is marked by bifurcations that create or annihilate pairs of fixed points in the phase space. As we will see in the next subsection, these fixed points bifurcations have a nontrivial effect on the phase space portrait. In what follows we treat the Larmor radius as an independent bifurcation parameter and explore the dependence of the dynamics on its value. However, it is important to keep in mind that on physical grounds the Larmor radius cannot have an arbitrary large value. Depending on the specific problem under consideration, there will be an upper bound of the Larmor radius which might limit the types of bifurcations occurring. Also, for very large values of ρ, the gyro-average approximation might require higher order corrections.

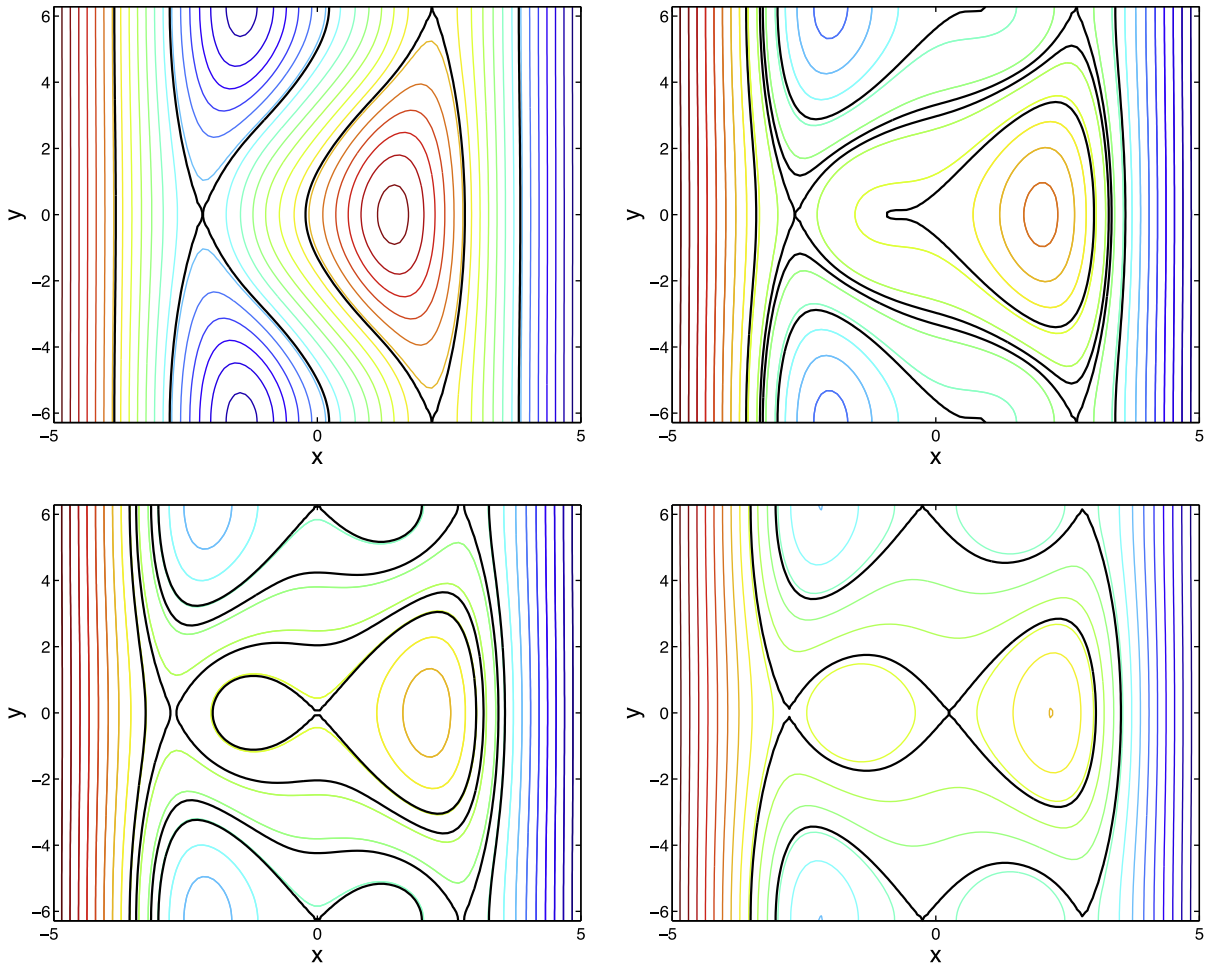

Fig. 8. Fixed points creation and separatrix reconnection. The four panels show contour plots of the gyroaveraged Hamiltonian in Eq. (27) with $\epsilon_1 = 0.5$, $\eta = 0.3$, $k = 0.5$ and increasing values of ρ. The bold black line denotes the contour level of the separatrix. Top-left panel corresponds to $\rho = 1.5$ which is in region I of Fig. 6; Top-right panel corresponds to $\rho = 2.204$ which is at the boundary between region I and region II in Fig. 6. Bottom left corresponds to $\rho = 2.3312$ which is in region II of Fig. 6. Bottom right corresponds to $\rho = 2.43$ which is in region II of Fig. 6.

4.2. Separatrix reconnection

When FLR effects are not included, the structure of the phase space is well-understood [7]. For a monotonic zonal flow in presence of one mode there is a single resonance which produces a chain of islands in the phase space as illustrated in Fig. 2. However, for a non-monotonic zonal flow, there can be two resonant points for a given mode, producing two chains of islands in phase space as shown in Fig. 3. Depending on the closeness of the resonances and the wave amplitude, there can be an overlap that changes the separatrix topology from heteroclinic (in which the separatrix joins different fixed points) to homoclinic (in which a branch of the separatrix joins the same fixed point).

The inclusion of FLR effects leads to several interesting new phenomena. The FLR effects on the heteroclinic topology are shown in Fig. 7. Starting from $\rho = 0$, it is observed that an increase in ρ can give rise to the standard hetroclinic-homoclinic bifurcation. However, as the last panel in Fig. 7 shows, at large enough values of ρ, dipole-type structures can appear. In this case, there are fixed points with $y_* \neq n\pi/k_1$. As discussed before, a change in ρ can give rise to the creation and annihilation of fixed points. To explore the consequences of these bifurcations on separatrix reconnection, Figs. 8 and 9 show contour plots of the one-mode, gyroaveraged nontwist Hamiltonian in Eq. (27) for values of ρ across the four regions in Fig. 6. In region I, there are two fixed points in x for each value of y_*. This is the familiar nontwist case in which the separatrix topology can be heteroclinc or homoclinic. However, crossing to region II creates two additional fixed points, and a total of four fixed points in x for each y_* are involved in determining the separatrix topology. As shown in Figs. 8 and 9 in this case the separatrix can exhibit a complex reconnection pattern. The transition to regions III and IV in Fig. 9 is accompained by the annihilation of fixed points that manifests in the formation of cusps in the corresponding contour lines of the the Hamiltonian. Finally, for parameter values in region IV, there are no fixed points and, as shown in the bottom left panel in Fig. 9, the trapping regions disappear. Fig. 10 illustrates the possibility of double heteroclinic–homoclinic separatrix reconnection for parameter

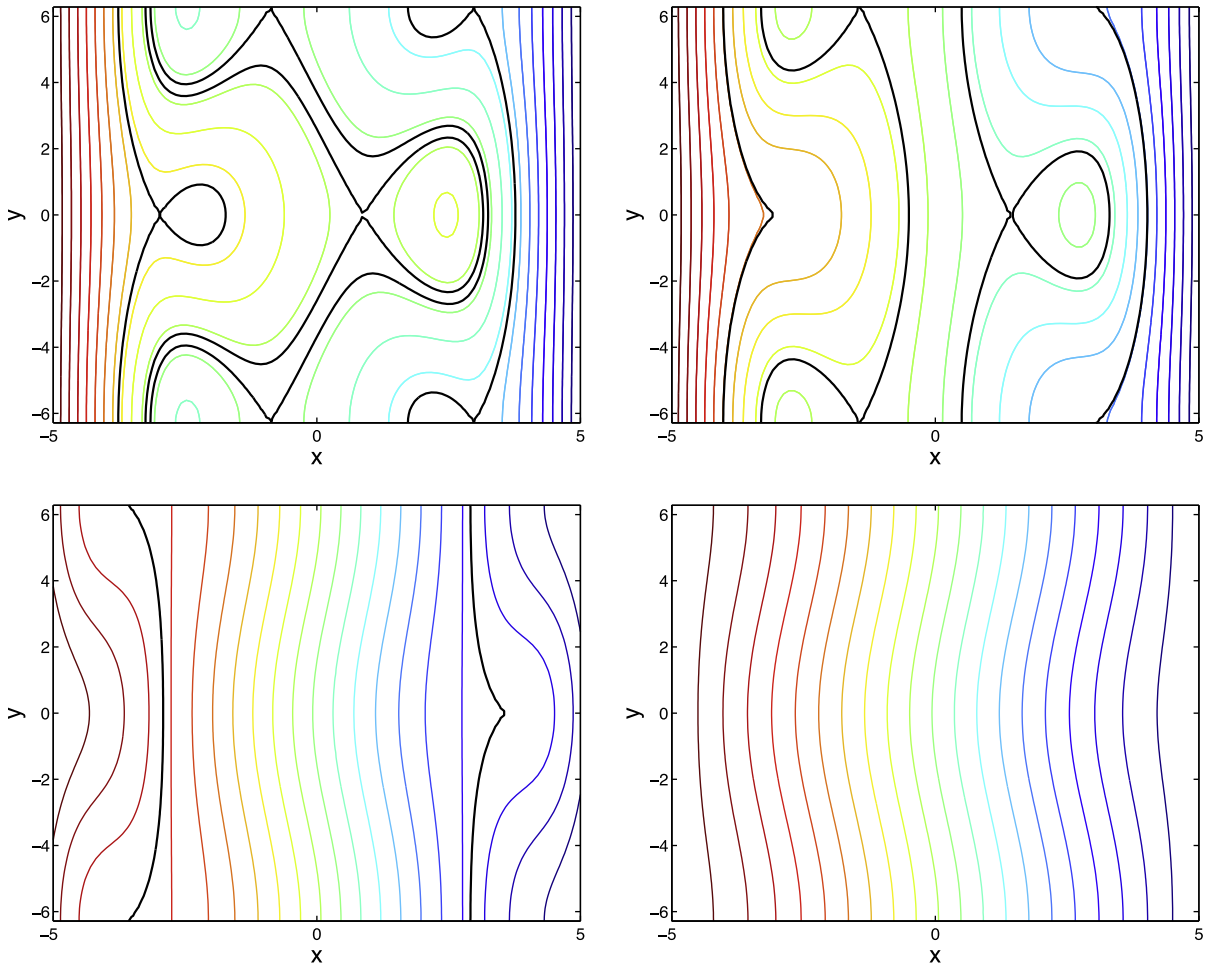

Fig. 9. Fixed points anhilation and flow rectification. The four panels show contour plots of the gyroaveraged Hamiltonian in Eq. (27) with $\epsilon_1 = 0.5$, $\eta = 0.3$, $k = 0.5$ and increasing values of ρ. The bold black line denotes the contour level of the separatrix. Top-left panel corresponds to $\rho = 2.75$ which is in region II of Fig. 6; Top-right panel corresponds to $\rho = 3.0748$ which is at the boundary between region II and region III in Fig. 6. Bottom left corresponds to $\rho = 4.464$ which is at the boundary between rgion III and IV of Fig. 6. Bottom right corresponds to $\rho = 6$ which is in region IV of Fig. 6.

values with four fixed points in x for each value of y_* as it is the case in region II of Fig. 6. Note that in this case, as the two panels at the bottom of Fig. 10 show, the island chains can be in phase.

4.3. Chaos supression

FLR can also have a nontrivial effect on the degree of chaos in the non-integrable ($\epsilon_1 \neq 0$ and $\epsilon_2 \neq 0$) regimen. To study this problem, we integrated numerically the gyroaveraged equations of motion in Eq. (18). The main result is that the FLR can lead to a suppression of chaos. By chaos suppression we mean an increase of the set of initial conditions for which invariant circles exist. Using the Lyapunov exponent as a measure of chaos, chaos suppression implies a reduction of the phase space regions with positive Lyapunov exponent. Here we limit attention to a qualitative description of this novel results using Poincare plots as the diagnostic tool. As Fig. 11 shows, increasing the Larmor radius can restore invariant circles and, for large enough ρ, make the system close to integrable. Of particular interest are the Poincare plots in Fig. 12 that show that increasing ρ can restore the shearless invariant circle. Although these results qualitatively indicate that increasing ρ tends to decrease chaos, it should be kept in mind that the exact threshold for the destruction of the shearless curve has a nontrivial dependence on ρ.

5. Summary and conclusions

We have presented a study of finite Larmor radius effects on $\mathbf{E} \times \mathbf{B}$ test particle chaotic transport in zonal flows with drift waves. The electrostatic potential was modeled as a linear superposition of a zonal flow and regular neutral modes of the

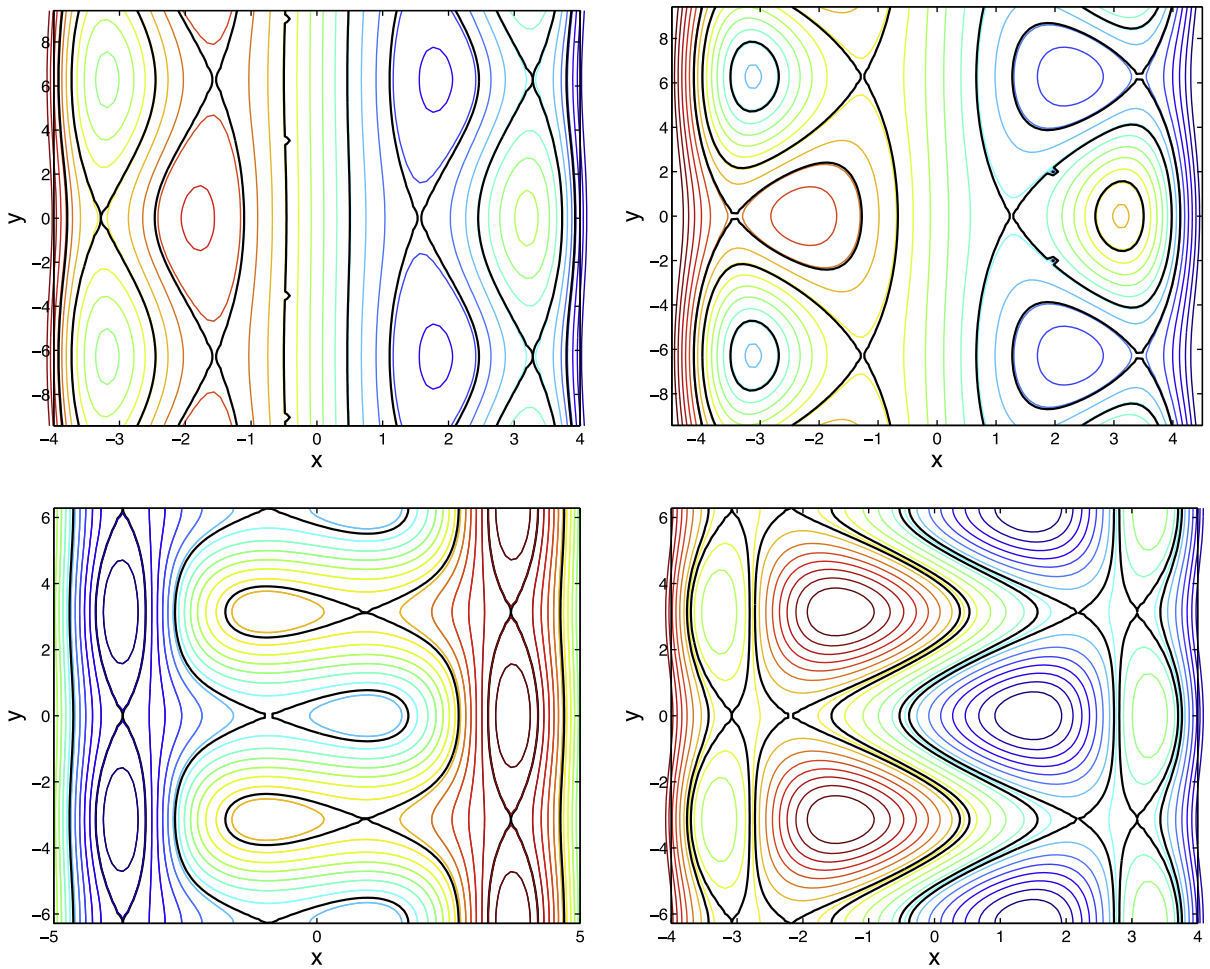

Fig. 10. Double separatrix reconnection and double dipole formation. The four panels show contour plots of the gyroaveraged Hamiltonian in Eq. (27). The bold black lines denote the contour values corresponding to the separatrix. Top-left panel: double heteroclinic topology for $\epsilon_1 = 0.075$, $\eta = 0.25$, $k = 0.5$ and $\rho = 3.25$. Top-right panel: double homoclinic topology for $\epsilon_1 = 0.3$, $\eta = 0.25$, $k = 0.5$ and $\rho = 3.25$. Bottom-left panel: double heteroclinic–homoclinic topology for $\epsilon_1 = 0.25$, $\eta = 0.2$, $k = 1$ and $\rho = 3.5$. Bottom-right panel: double dipole formation for $\epsilon_1 = 0.2$, $\eta = 0.25$, $k = 1$ and $\rho = 3.25$.

Hasegawa–Mima equation. FLR effects are incorporated by gyro-averaging the $\mathbf{E} \times \mathbf{B}$ Hamiltonian. We focused attention on non-monotonic zonal flows for which the corresponding $\mathbf{E} \times \mathbf{B}$ Hamiltonian does not satisfy the twist condition. Non-twist Hamiltonians exhibit global changes in the phase space known as separatrix reconnection. In addition, in these Hamiltonians, shearless curves provide robust barriers to chaotic transport. In this paper we studied the role of FLR effect on both, separatrix reconnection and chaotic transport. A bifurcation of the zonal flow was observed as the Larmor radius increases. There is a critical value for which the zonal flows transitions from a profile with one maximum to a profile with two maxima and a minimum. This bifurcation leads to the creation of additional shearless curves which form at the extrema of the zonal flow profile. The zonal flow bifurcation has also an impact on the formation of additional resonances, i.e. regions where the frequency of the perturbation matches the frequency of the zonal flow. In the presence of only one normal mode the Hamiltonian is integrable, and because of the violation of the twist conditions, the single-mode Hamiltonian exhibits sepratrix reconnection. The gyroaveraged Hamiltonian exhibits vey complex changes in the phase space depending on the Lamor radius. A change of the Larmor radius can lead to heteroclinic–homoclinic bifurcations and dipole formation. For Larmor radii for which the zonal flow has bifurcated, we have observed double heteroclinic–heteroclinic, homoclinic–homoclinic and heteroclinic–homoclinic topologies. As the Larmor radius increases we have observed the formation and annihilation of fixed points in the phase space. For large enough Larmor radius all fixed points disappear and the phase space of the integrable, one-mode gyroaveraged Hamiltonian does not exhibit any resonances.

The role of FLR effects on chaotic transport in the presence of two drift waves was also considered. The main conclusion is that chaos is typically reduced as the Larmor radius increases. Poincare sections show that, for large enough Larmor radius, chaos can be practically suppressed. In particular, small changes on the Larmor radius can restore the shearless curve. The

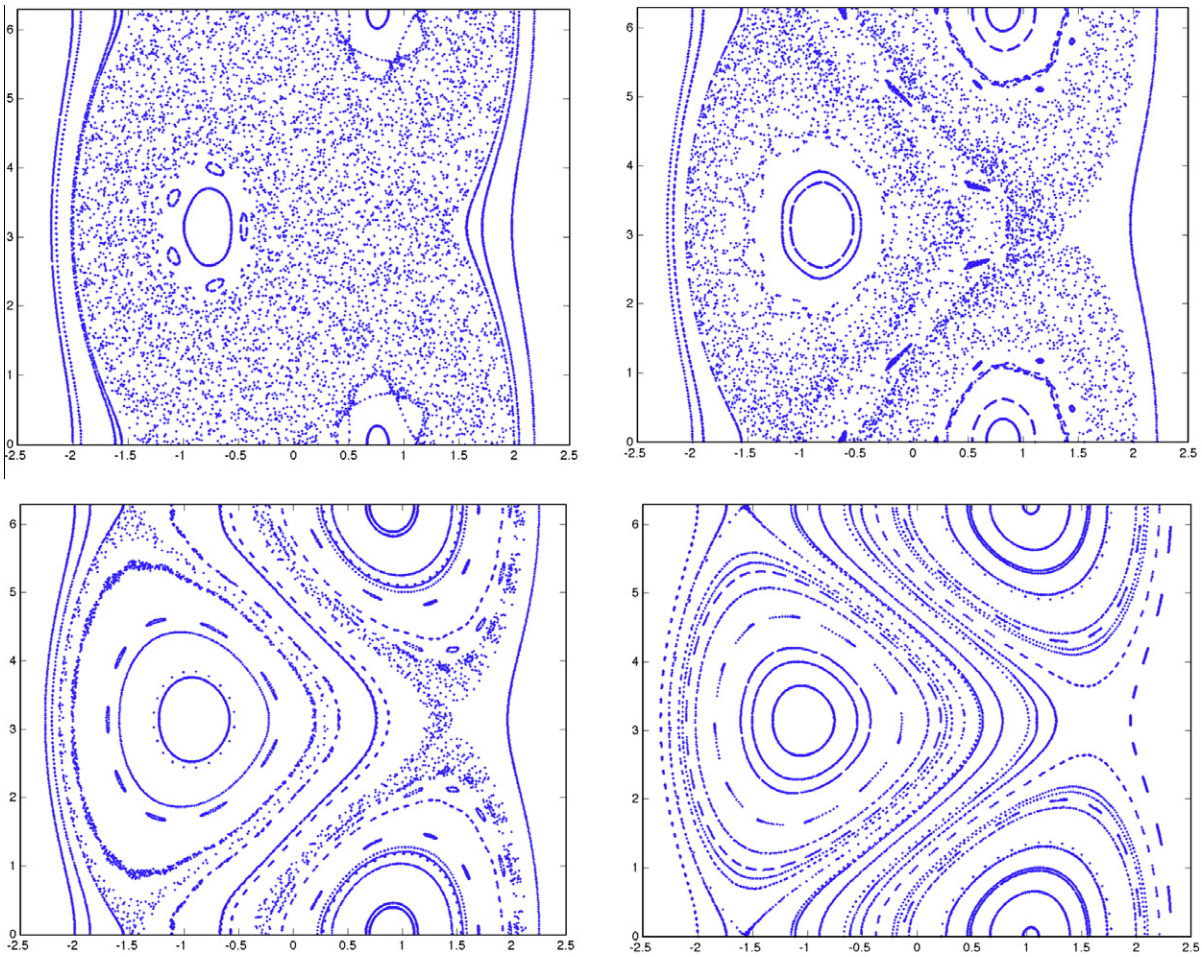

Fig. 11. Chaos suppression due to gyroaveraging. The four panels show Poincare plots for the gyroaveraged Hamiltonian system in Eq. (18) with $\epsilon_1 = \epsilon_2 = 0.5$, $k_1 = k_2 = 1$, $\eta = 0.4$ and: $\rho = 0$ (top left panel), $\rho = 0.5$ (top right panel), $\rho = 0.75$ (bottom left panel), and $\rho = 1$ (bottom right panel).

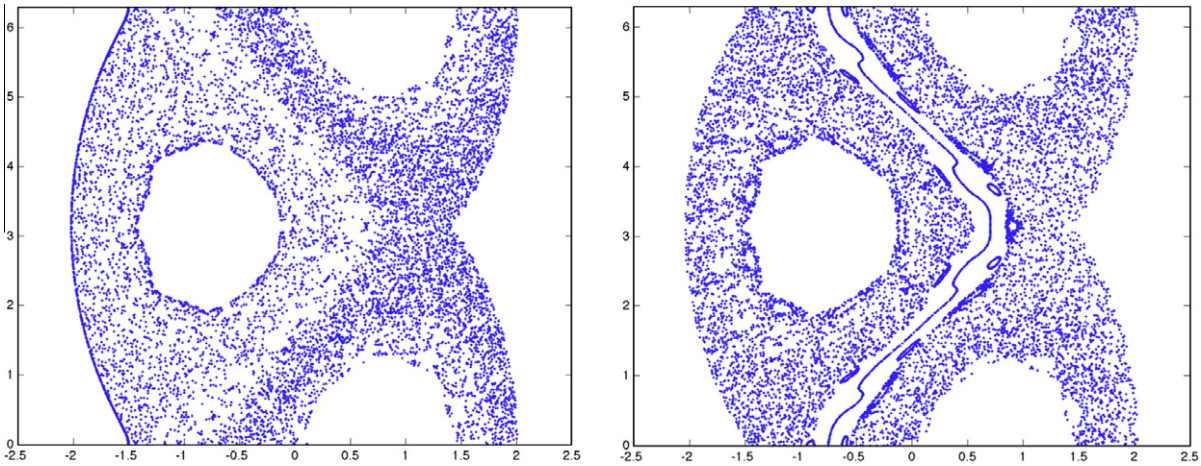

Fig. 12. Shearless curve recovery due to gyroaveraging. The two panels show Poincare plots for the gyroaveraged Hamiltonian system in Eq. (18) with $\epsilon_1 = 0.5, \epsilon_2 = 0.25$, $k_1 = k_2 = 1$, $\eta = 0.4$ and: $\rho = 0.4$ (left panel), $\rho = 0.5$ (right panel). The increase of the Larmor radius leads to the recovery the shearless curve going through $(x,y) \approx (-0.75, 0)$, and the suppression of global transport across the resonances.

onset of global chaos typically tends to increase with the Larmor radius. However, preliminary calculations indicate that the threshold for the destruction of the shearless curve exhibits a complex dependence on the Larmor radius.

Acknowledgments

This work was sponsored by the Oak Ridge National Laboratory, managed by UT-Battelle, LLC, for the U.S. Department of Energy under contract DE-AC05-00OR22725, and by projects PAPIIT-UNAM IN119408 and Conacyt 81232, Mexico. DdCN gratefully acknowledges the hospitality of the Institute for Nuclear Sciences at UNAM, Mexico City during part of the elaboration of this project.

References

[1] del-Castillo-Negrete D, Morrison PJ. Bull Am Phys Soc Ser II 1992;37:1543.
[2] Davidson MG, Dewar RL, Gardner HJ, Howard J. Aust J Phys 1995;48:871.
[3] Hayashi T, Sato T, Gardner HJ, Meiss JD. Phys Plasmas 1995;2:752.
[4] Oda GA, Caldas IL. Chaos Solit Fract 1995;5:15.
[5] Balescu R. R Phys Rev E 1998;58:3781.
[6] Firpo MC, Constantinescu D. Phys Plasmas 2011;18:032506.
[7] del-Castillo-Negrete D, Morrison PJ. Phys Fluids 1993;A5:948.
[8] Beron-Vera FJ, Olascoaga MJ, Brown MG MG, et al. Chaos 2010;20:017514.
[9] Uleysky MY, Budyansky MV, Prants SV. Phys Rev E 2010;81:017202.
[10] Karney CFF. Phys Fluids 1978;21:1584.
[11] Abdullaev SS. Chaos 1994;4:569.
[12] Kaufman IK, Luchinsky DG, McClintock PVE, Soskin SM, Stein ND. Phys Lett A 1996;220:219.
[13] Kim JH, Lee HW. Phys Rev E 1995;52:473.
[14] del-Castillo-Negrete D, Firpo MC. Chaos 2002;12:496.
[15] Horton W, Park HB, Kwon JM, Strozzi D, Morrison PJ, Choi DI. Phys Plasmas 1998;5:3910.
[16] del-Castillo-Negrete D. Phys Plasmas 2000;7:1702.
[17] Marcus FA, Caldas IL, Guimaraes-Filho ZO, Morrison PJ, Horton W, Kuznetsov YuK, et al. Phys Plasmas 2008;15:112304.
[18] Hasegawa A, Mima K. Phys Fluids 1978;21:87.
[19] Lee WW. J Comput Phys 1987;72:243.
[20] Brizard A, Hahm TS. Rev Mod Phys 2007;79:421.
[21] Manfredi G, Dendy R. Phys Rev Lett 1996;76:4360.
[22] Manfredi G, Dendy R. Phys Plasmas 1997;4:628.
[23] Annibaldi V, Manfredi G, Dendy RO. Phys Plasmas 2002;9:791.
[24] Gustafson K, del-Castillo-Negrete D, Dorland W. Phys Plasmas 2008;15:102309.
[25] Howard JE, Hohs SM. Phys Rev A 1984;29:418.
[26] van der Weele JP, Valkering TP. Physica A 1990;169:42.
[27] Howard JE, Humphreys J. Physica D 1995;80:256–72.
[28] del-Castillo-Negrete D, Greene JM, Morrison PJ. Physica D 1996;91:1.
[29] Wurm A, Apte A, Fuchss K, Morrison PJ. Chaos 2005;15:023108.
[30] del-Castillo-Negrete D, Greene JM, Morrison PJ. Physica D 1997;100:311.
[31] Fuchss K, Wurm A, Apte A, Morrison PJ. Chaos 2006;16:033120.
[32] Szezech Jr JD, Caldas L, Lopes SR, Viana RL, Morrison PJ. Chaos 2009;19:043108.
[33] Delshams A, de la Llave R. SIAM J Math Anal 2000;31:1235.
[34] Simo C. Regul Chaotic Dyn 1998;3:180.
[35] Shinohara, Aizawa Y. Prog Theor Phys 1997;97:379.
[36] Arnold VI. Mathematical methods of classical mechanics. New York: Springer-Verlag; 1978.
[37] Moser J. Stable and random motion in dynamical systems. Princeton, NJ: Princeton University Press; 1973.
[38] Greene JM. J Math Phys 1979;20:1183.